Screen-printed Nickel Oxide Nanoparticles and Microballs as Efficient Water Oxidation Catalysts: Comparison of Catalytic Activity and Impedance Behaviour

Archana Singh*,[a,b,c] Monika Fekete,[a,b] Thomas Gengenbach,[d] Alexandr N. Simonov,[a,b] Rosalie K. Hocking,[a,b,e] Shery L. Y. Chang,[a] Mathias Rothmann,[f] Satvasheel Powar,[a] Dongchuan Fu,[f] Zheng Hu, [g] Qiang Wu, [g] Yi-Bing Cheng, [f, g] Udo Bach,[f,d,h] and Leone Spiccia*[a,b]

Abstract: We report that films screen-printed from nickel oxide (NiO) nanoparticles and microballs are efficient electrocatalysts for water oxidation under near neutral and alkaline conditions. Investigations of the composition and structure of the screen-printed films, by XRD, XAS and SEM, confirmed that the material was present as the cubic NiO phase. Comparison of the catalytic activity of the microball films to that of films fabricated using nickel oxide nanoparticles, under similar experimental conditions, revealed that the microball films outperform nanoparticle films of similar thickness due to a more porous structure and higher surface area. A thinner, less resistive NiO NP film, however, was found to have higher activity per Ni atom. Anodization in borate buffer significantly improves the activity of all three films. XPS analysis showed that during anodization, a mixed nickel oxy-hydroxide phase formed on the surface of all films, which could account for the improved activity. Impedance spectroscopy revealed that surface traps contribute significantly to the resistance of the NiO films. On anodization the trap state resistance of all films is reduced leading to significant improvements in activity. In 1.00 M NaOH, both the microball and nanoparticle films exhibit high long-term stability and produce a stable current density of ~30 mA/cm^2 at 600 mV overpotential.

Introduction

The potential of solar water splitting ($2H_2O \rightarrow O_2 + 2H_2$) to provide a cheap and abundant source of renewable energy is stimulating interest in the development of materials that catalyze two key processes; water oxidation and proton reduction.[1,2] In recent years, water oxidation catalysts based on cheap and abundant first row transition series metal ions, such as Mn, Fe, Co and Ni have been attracting much attention. [3-27] Among the materials from first row transition series metal ions, nickel oxy-hydroxides have been shown to be very promising electrocatalysts.[3,6,28-33] Nocera and co-workers recently reported the electro-deposition of γ-NiOOH from borate buffered aqueous Ni^{2+} solutions (pH = 9.20)[3] and showed that the films oxidized water at moderate overpotentials.

We recently demonstrated that uniform nickel oxy-hydroxide films can be electrochemically deposited from solutions of the tris(1,2-diaminoethane)nickel(II) complex, $[Ni(en)_3]^{2+}$.[34] These films were shown to have higher electroactive surface area and catalytic activity relative to the corresponding films derived from Ni^{2+} under similar experimental conditions.[34] In general, the nickel oxide films used as water oxidation catalysts have been deposited using either electrochemical or sol-gel methods.[31-33] Although these methods are facile, electrodeposition can suffer from a non-uniform rate of mass transport to the electrode surface resulting in the growth of inhomogeneous films, and it can also be difficult to control film thickness where catalysis and deposition occur in parallel. Sol-gel processing is often limited in the thickness of films that can be deposited and the films may not necessarily be ideal for catalytic applications. Screen-printing, on the other hand, is a cost effective alternative for fabricating films with controlled thickness and area with high reproducibility. We, and others, have shown that manganese oxides can be efficiently screen-printed and exhibit excellent water oxidation activity over a variety of experimental conditions.[14, 35]

Screen-printed nickel oxide microball films with high surface area and optimum optical properties have been successfully implemented in p-type dye sensitized cells and have been shown to achieve photocurrent densities of 7 mA/cm^2 under one sun light intensity.[35] To the best of our knowledge, however, screen-printed nickel oxide films have not been studied as electrocatalysts for the water oxidation reaction. Here, we report an investigation of the catalytic activity of screen-printed nickel oxide in which the films derived from microballs (NiO-MB) and nanoparticles (NiO-NP) are compared under similar experimental conditions. The composition, structure and morphology of the screen printed films have been studied by scanning electron microscopy (SEM), transmission electron microscopy (TEM), X-ray photoelectron spectroscopy (XPS), powder X-ray diffraction (XRD), X-ray absorption spectroscopy (XAS), Brunauer-Emmett-Teller (BET) surface area analysis, electrochemical impedance spectroscopy (EIS) and the catalytic activity investigated by linear scan voltammetry (LSV), controlled potential electrolysis (CPE) and evolved oxygen quantification.

[a] Dr. A. Singh, Dr. M. Fekete, Dr. R.K. Hocking, Dr. S.L.Y. Chang, Dr. S. Powar, Prof. Dr. L. Spiccia
School of Chemistry, Monash University, Victoria, 3800 Australia.
E-mail: leone.spiccia@monash.edu, archanas002@gmail.com
[b] Dr. A. Singh,Dr. M. Fekete, Dr. R.K. Hocking, Prof. Dr. L. Spiccia
Australian Centre of Excellence for Electromaterials Science, Monash University, Victoria, 3800 Australia.
[c] Dr. A. Singh
Advanced Materials and Processing Research Institute, CSIR, Bhopal, India.
[d] Thomas Gengenbach,Prof. Dr. Udo Bach
Commonwealth Scientific and Industrial Research Organisation, Manufacturing Flagship, Clayton, Victoria 3168, Australia.
[e] Dr. R. K. Hocking
School of Chemistry, James Cook University, Townsville, Queensland,4811,Australia.
[f] Dr. D. Fu, Prof. Dr. Y. B. Chang, Prof. Dr. Udo Bach
Department of Materials Science and Engineering, Monash University, Victoria, 3800 Australia.
[g] Z. Hu, Q. Wu, Prof. Dr. Yi-Bing Cheng
Key Lab of Mesoscopic Chemistry of MOE, School of Chemistry and Chemical Engineering, Nanjing University, Nanjing 210093, China
[h] Prof. Dr. Udo Bach
Melbourne Centre for Nanofabrication, Clayton, Victoria 3168, Australia

Supporting information for this article is given via a link at the end of the document.

Results and Discussion

Nickel oxide microballs were synthesized by a thermolysis method as described earlier[35] whereas the nanoparticles were obtained commercially. The NiO microballs have a porous spherical morphology, with each sphere having a diameter of ca. 3 µm. Powder XRD measurements confirmed that both the NiO microballs and commercial powder have the cubic-NiO structure, in agreement with previous work.[27] The films were printed on FTO glass using a commercial semi-automatic screen-printer following an established procedure.[35] The thickness of a single layered NiO-MB film, measured using stylus profilometry, was 3.10 µm. For comparison, a NiO-NP film of similar thickness (2.80 µm) and the single layered NiO-NP1 films (thickness: 0.80 µm) was also printed (see Table 1). The surface area of the sintered NiO-MB was approximately 16% higher when compared to the sintered NiO-NP (Table 1).[35] Inductively coupled plasma-time of flight-mass spectrometry (ICP-TOF-MS) was used to quantify the amount of Ni present per cm^2 of geometric electrode area. Although the NiO-MB films are slightly thicker than the NiO-NP films, due to their more porous structure, they contain less Ni, 0.45 mg Ni/cm^2 compared to 1.10 mg Ni/cm^2 for the NiO-NP. The single layered NiO-NP1 film contained 0.33 mg Ni/cm^2.

Table 1: Turnover frequency (TOF), BET surface area[28]and calculated relative electrochemical surface areas for NiO-MB, NiO-NP and a thinner NiO NP film (NiO-NP1) before and after anodization in 0.60 M borate buffer solution (pH = 9.20).

Films	Thick-ness[a] (µm)	Ni content[b] (mg/cm^2)	O_2 production[c] (O_2/Ni/h)		BET s. area[d] (m^2g^{-1})	A_{echem}[e] (cm_e^2/cm_g^2)
			Fresh	Anod.		
NiO MB	3.2	0.45	8	10	65	292
NiO NP	2.8	1.1	6	8	56	610
NiO NP1	0.8	0.33	13	17	56	184

a) thickness was measured by profilometry. b) Ni content was measured by ICP-TOF-MS analysis c) oxygen production was measured in 0.60 M borate buffer (pH = 9.20), at 1.00 V *vs.* Ag/AgCl (η = 0.52 V) over 1 hour using a NeoFox fluorescence-quenching oxygen sensor. d) surface area was measured by BET analysis. e) A_{echem} was calculated based on BET and ICP-TOF-MS data: $A_{echem}[cm_e^2cm_g^{-2}]$ = Ni content [mg/cm_g^2] x BET surface area [cm_e^2/mg].

The three printed catalyst films were used to study catalytic activity in water oxidation. The catalytic activity in 0.60 M aqueous sodium borate buffer solution was assessed by linear scanning voltammetry (LSV), at a scan rate of 20 mV/s, in a standard three electrode cell comprising the NiO films as working electrodes, a Pt counter electrode and an Ag|AgCl|KCl(3 M) (herein after, Ag/AgCl) reference electrode. The films were tested as freshly made (Fig.1, full lines) and were then subjected to constant potential electrolysis for 12 h at an overpotential for water oxidation of *ca* 0.62 V (1.10 V vs Ag/AgCl at pH = 9.20). {η; calculated as a difference between the potential applied to the electrode and the standard electrode potential for the water oxidation reaction, which is pH-dependent according to E^0 = 1.23 - 0.059·pH V *vs.* normal hydrogen electrode}.This treatment is further referred to as anodization, or electrode ageing, and typical current transients are shown in the insets of Figs. 1 and 2. The activities of the anodized films were then once again tested by LSV (Fig.1, dashed lines). To compare the catalytic efficiencies of the three films in terms of catalytic activity per Ni centre, the results of the electrochemical performance analysis are presented here both scaled to the geometric electrode surface area (Fig. 1A) and to the Ni content of each film (Fig. 1B). The LSV scans of the three fresh films show an onset potential for water oxidation at around 0.90 V vs Ag/AgCl (corresponding to η of ~0.42 V) right after a voltammetric peak associated with oxidation of the surface-confined Ni^{2+}species.[6] Fig. 1A shows that the highest activity was achieved by the NiO-NP film, followed by the thin NiO-NP1 film, while the NiO-MB film had the lowest activity when scaled to geometric surface area. In comparison, per Ni atom, the thin NiO-NP1 film achieved the highest activity (Fig 1B). This implies that, while thicker films benefit from a larger electrochemical surface area, this advantage is outweighed by an increase in film resistance and/or hindered mass-transport. This supposition is in agreement with Bell *et al* who reported that the catalytic activity of nickel oxy-hydroxide films, deposited on a gold substrate, decreases sharply with increasing film thickness.[39] Dyer also discussed that a denser loading of the NiO may cause a blockage effect that is reflected in a decrease in the catalytic efficiency as the NiO_x loading increases.[40]

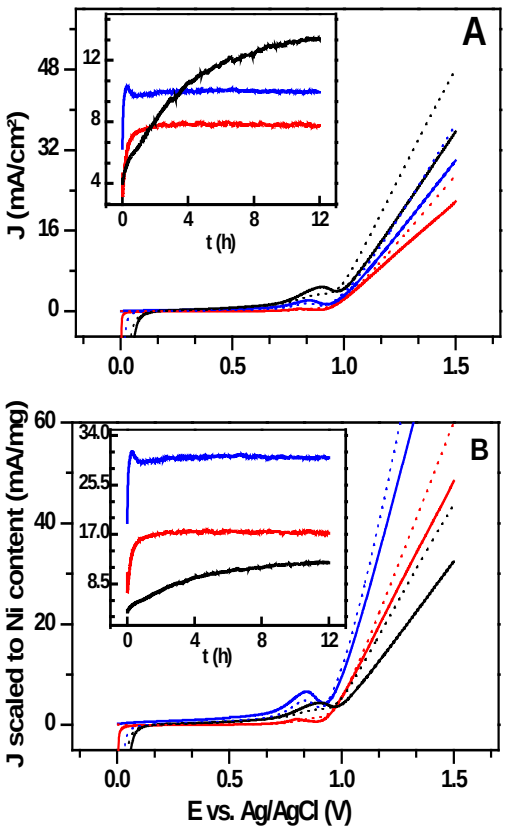

Figure 1: a) LSV of fresh NiO-MB (red full line), NiO-NP (black full line), NiO-NP1 (blue full line), anodized NiO-MB (red dashed line), anodized NiO-NP (black dashed line) and anodized NiO-NP1 films in 0.60 M borate buffer recorded at scan rate of 20 mV/sec. Inset shows the CPE graph for NiO-MB, NiO-NP and NiO-NP1 films in 0.60 M borate buffer (pH = 9.20) at 1.10 V *vs.* Ag/AgCl (η = 0.62 V) continuously for 12 h. B) Data in Fig. 1A is shown scaled against the nickel content of each film.

The NiO-MB film outperformed the NiO-NP film of similar thickness. A possible reason for this could be that more Ni centers are accessible to the water substrate in the porous NiO-MB film, also that the protons generated from water

oxidation can be transported away from the reaction centers more efficiently by the buffer solution than in the case of the compact NiO-NP film. The activity of NiO_x films has previously been shown to increase significantly on anodization due to the conversion of the nickel oxide into a phase that is more active in water oxidation catalysis.[3] To examine whether anodization affects the catalytic activity of these NiO films, long term testing of the NiO-MB, NiO-NP and NiO-NP1 electrodes was performed at 1.10 V *vs* Ag/AgCl in 0.60 M borate buffer (pH = 9.20), which corresponds to η = 0.62 V, for a continuous period of 12 h (insets of Fig. 1A and Fig. 1B). It is clear from the data that the water oxidation current recorded for the NiO-MB films nearly doubled in the first hour and was found stable over the rest of the 12 h testing period. Similarly, the activity of the NiO-NP1 films increased rapidly in the first hour (by ca. 50%), and then stabilized.

The current density obtained from the NiO-NP films increased significantly over a period of about 8 h of CPE, and resulted in a 3-fold improvement in activity (see Figure 1A inset). The anodization current profile of the NiO-NP film may have differed from that for the other two films because of the larger amount of nickel oxide present in the compact film, and a slower transformation to a catalytically more active phase. Partial oxidation of the films is further indicated by a diminution of the oxidation peaks clearly visible in the LSV scans of all fresh films just below the onset potential (around 0.80 V vs. Ag/AgCl). Phase transformation to a mixed nickel oxide-hydroxide was later confirmed by XPS studies (see below). Importantly, the robustness of the screen-printed films under extended testing is demonstrated by the fact that the films functioned as water oxidation catalysts continuously for twelve hours producing highly stable currents.

To confirm that the observed current is due to water oxidation, the amount of evolved oxygen by a NiO MB film was measured using an Ocean Optics fluorescence-based oxygen sensor. Over a period of one hour, at pH 9.20 and applied bias of 1.10 V (*vs.* Ag/AgCl) enough charge was passed to produce 7.70 µmole of oxygen, whereas 7.20 µmole was measured experimentally, corresponding to a Faradaic efficiency of 94 % (SI Fig. S1). The Tafel slopes, determined by stepwise chronoamperometry (SI, Fig. S2), were found to be 111 ± 2, 116 ± 2 and 99 ± 2 mV/decade for the NiO-MB, NiO-NP and NiO-NP1 films, respectively. These results are in agreement with those reported previously for active nickel oxide electrocatalysts (~120 mV/decade).[32,34]

The fact that NiO_x films are efficient water oxidation catalysts in alkaline media led to an assessment of the performance of the NiO-MB and NiO-NP films in 1.00 M NaOH (Fig. 2).[31,39,41] The LSVs of the NiO-MB and NiO-NP films show an onset of water oxidation at 0.60 V vs. Ag/AgCl, which corresponds to an overpotential of ca 0.35 V, a significant reduction compared to η = 0.41 V in the pH 9.20 borate buffer (Fig. 2A and 2B). In a controlled potential electrolysis experiment at η of ~0.60 V (0.80 V vs. Ag/AgCl in 1.00 M NaOH) stable current densities of 29 and 33 mA/cm^2 were measured over hours for the NiO-MB and NiO-NP1 films respectively (see Fig 2A, inset), this corresponds to TOFs of 15 and 18 (molecules of oxygen produced per Ni center per hour) of NiO-MB and NiO-NP1. NiO-NP1 films were further tested as water oxidation catalyst for continuous 12 h of operation at overpotential of 0.60 V in 1.00 M NaOH electrolyte solution (Fig. S3). Thus, the films showed a similar trend in the NaOH electrolyte solution as obtained in the borate buffer, with the thin NiO-NP1 films again exhibiting the highest activity per Ni atom (Fig. 2B). Importantly, compared to pH 9.20, the films produced much higher current densities and an approximate 10-fold increase in the TOF at a similar overpotential. The CPE experiments (Fig 2A and B, insets, Fig. S3) also illustrate the good stability of the NiO films. The current density measured for the NiO-MB film slightly increased up to one hour of operation and then became stable. The NiO-NP1 films were stable in their performance for at least 12 hours (Fig. S3). These observations highlight the benefits of screen printing method for the fabrication of thin catalyst films for water oxidation and other applications.

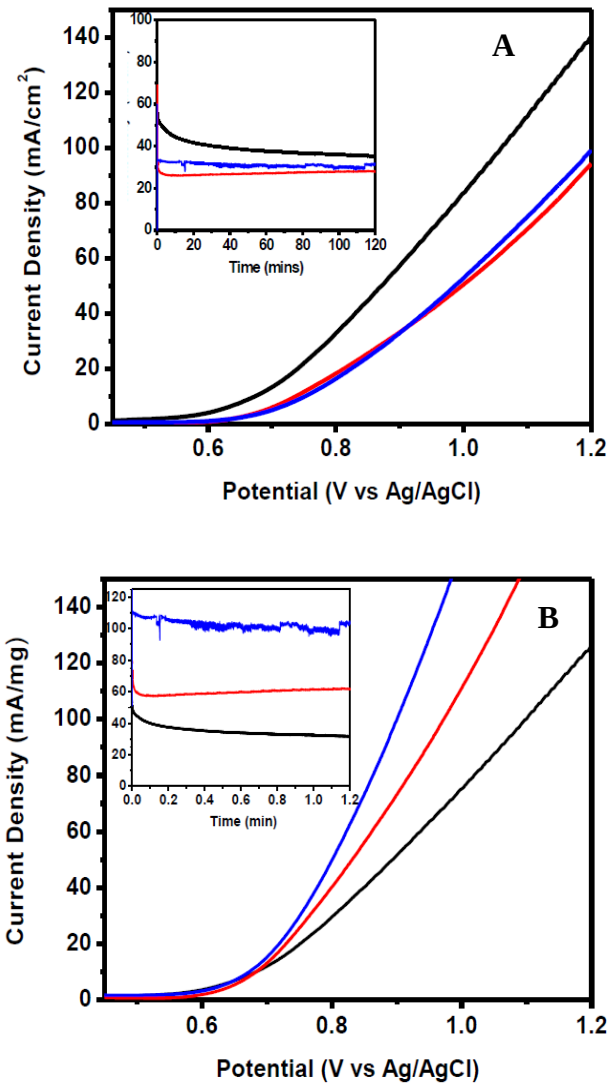

Figure 2: (A): LSV of NiO-MB (red), NiO-NP (black) and NiO-NP1 (blue) films in 1.00 M NaOH recorded at 1.00 mV/s. (B) LSV data in A scaled against the Ni content of films. Inset shows the CPE for NiO-MB (red), NiO-NP (black) and NiO-NP1 (blue) films in 1.00 M NaOH recorded at 0.80 V *vs*. Ag/AgCl (η of *ca* 0.60 V).

The morphology of the screen-printed NiO films was studied by SEM and TEM. The SEM images of the fresh NiO-MB and NiO-NP films (shown in Fig. 3A and 3C) indicate significant differences in film structure. The NiO-MB film consists of thin flakes with a lace-like fine structure, whereas the NiO-NP film is composed of agglomerated nanoparticles (diameter, $d \approx 25$ nm). In addition, the morphology of the NiO-MB film differs significantly from that of the powder form. Previous SEM studies have shown that the NiO-MB powder consists of a well-defined porous spherical structure,[28,35] which, in the case of the currently presented NiO-MB film, was replaced by a flake-like structure (Fig. 3A). This change in morphology occurred during ball milling of the NiO-MB

powder, which forms part of the preparation of the screen-printing paste, as described above. The SEM images recorded after 12 hrs of operation (Fig. 3B and 3D) show a small degree of surface corrosion in the case of the NiO-MB films. No significant changes were observed on the NiO-NP film surface, confirming the chemical and mechanical stability of the films. The XRD patterns of the fresh screen-printed films (shown in Fig. S4) are consistent with the cubic NiO phase with characteristic peaks at the 2θ angles of 37.3°, 43.4°, 63.0°, 75.6° and 79.6° identified as the [111], [200], [220], [311] and [222] plane for cubic NiO crystallites, respectively.[42] The predominance of the cubic NiO phase for all films (fresh and anodized) was also confirmed by HR-TEM (Fig S5). The measured lattice spacings based on electron diffraction patterns showed a good match in each case with the JCPDS 73-1519 cubic NiO standard.

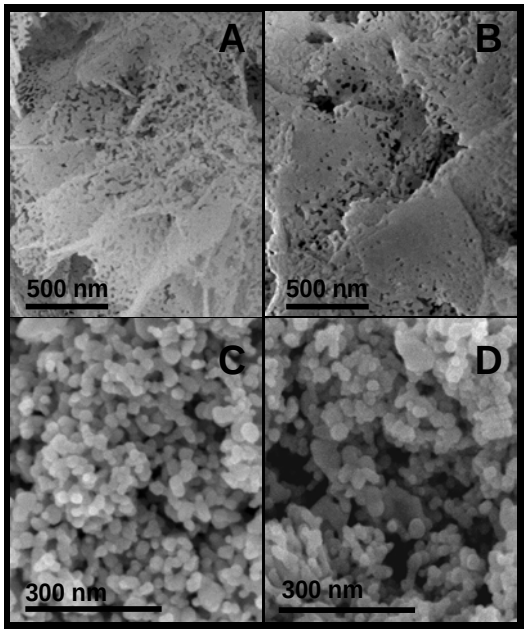

Figure 3: SEM images of the fresh NiO-MB (A) and NiO-NP (C) films recorded at working distance of 5 mm. The B and D panels show SEM images of the NiO-MB and NiO-NP films, respectively, recorded after twelve hours of catalytic operation in a 0.60 M borate buffer.

Ex situ nickel K-edge X-ray absorption spectroscopy (XAS) of the freshly prepared NiO-MB and NiO-NP films (see Fig. 4) were also consistent with the cubic NiO structure (SI Fig. S6).[17] A comparison of the LSV of the anodized and non-anodized film (Fig. 1A and B) clearly shows an improvement in current density on anodization (films were subjected to anodization in borate buffer for 12 h at overpotential of 0.62 V) and a reduction of the onset of catalysis by 80-100 mV. However, the XANES (Fig. 4), XRD and EXAFS (Fig. S4 and Fig. S6) of the fresh and anodized NiO-NP and NiO-MB films revealed no significant change in the spectra after anodization indicating that there is no bulk phase transformation had occurred and the XRD peak at 2θ = 43.1°(characteristic of cubic NiO) is still present even after prolonged testing.

To test if a phase change, accounting for the observed improvements in catalytic activity, could have occurred on the surface of the NiO particles during water oxidation, the fresh and anodized films were analyzed by XPS. XPS analysis revealed that, contrary to the bulk of the films, the surface layer of both the nanoparticle and the microball films transformed into a mixed nickel oxide-hydroxide phase after electrocatalytic studies in borate buffer and NaOH solutions. Figs. 5 and S7 show the corresponding characteristic change of the Ni 2p spectra as described and discussed by Biesinger et al. [43] In the case of pure NiO, the main portion of the Ni $2p_{3/2}$ spectrum consists of a sharp narrow peak at a binding energy (BE) of 854.6 eV and a broader component at approx. 855.5 eV whereas for $Ni(OH)_2$ the same spectral region does not display the narrow, lower BE peak but only a single broad peak at the higher BE.[43] Our data clearly show a significant loss of intensity of the peak at 853.6 eV relative to the component at 855.5 eV after anodization. The fact that the lower BE peak had not completely disappeared indicates that both, Ni hydroxide as well as NiO, were present at the surface (within the XPS sampling depth of 5-10 nm). The corresponding O 1s spectra are shown in Fig. S8.Determination of the surface compositions by XPS provided additional evidence for this chemical surface change. For the films subjected to 12 h anodization in the borate buffer solution, the O/Ni atomic ratio increased from 0.94 (NiO-NP) and 0.93 (NiO-MB) to 1.40 and 1.24, respectively, after anodization. In NaOH, this ratio increased from 0.94 to 2.00 for the NiO-NP1 sample after continuous water oxidation at η = 0.60 V for 12 h. Since Conway, Nocera and others have found that [3,4,6,9,28-33] nickel oxy-hydroxide is a highly active catalyst in water oxidation, it is likely that even a thin layer of the nickel oxy-hydroxide could result in a significant improvement in the catalytic activity.

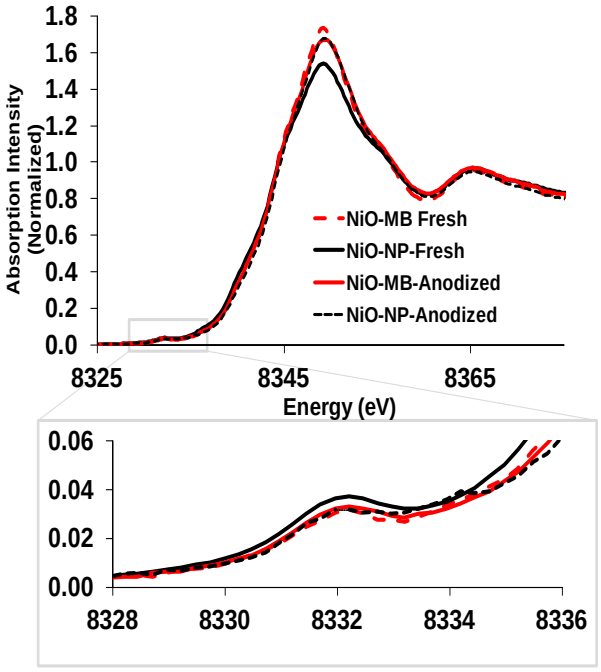

Figure 4: XANES (top) and pre-edge (bottom) XAS of fresh and anodized NiO-MB (red bold, red dashed line) and NiO-NP (black bold, black dashed) films. Anodization was done in 0.60 M borate buffer at pH 9.20.

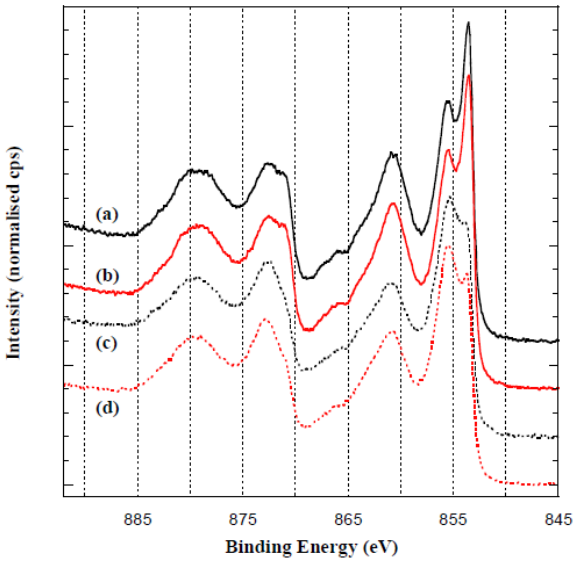

Figure 5: XPS Ni 2p spectra of (a) NiO-NP (black), (b) NiO-MB (red), (c) NiO-NP anodized at pH =9.20 in 0.60 M borate buffer (black, dashed line), and (d) Ni-MB anodized at pH = 9.20 in in 0.60 M borate buffer (red, dashed line) films. See text for details.

The origin of the difference in the catalytic activity of the NiO-NP, NiO-NP1 and NiO-MB films was further investigated by electrochemical impedance spectroscopy (EIS). EIS is a powerful tool that can be used to extract information about the origin and factors contributing to the total Ohmic resistance involved in the water oxidation reaction, ultimately determining its efficiency. Therefore, to improve the overall efficiency by identifying resistance bottlenecks, it is essential to establish an equivalent circuit (EC) that can be used to model the charge transfer processes in the electrochemical cell. Bisquert and co-workers, applying an EC similar to that pictured in Figure 6, demonstrated the role of surface states in the water oxidation using hematite electrodes.[44] The surface hole collection efficiency was shown to approach unity, when a fast hole collector (the ferrocene$^{0/+}$ redox couple) in acetonitrile was used. In contrast, the holes accumulated in the depletion layer of the semiconductor film were transferred more sluggishly to the water molecules in aqueous solutions. In this case, surface states were identified as recombination centres, trapping holes from the valence band and electrons from the conduction band. The presence of such surface traps can easily be determined by carrying out current transients on the catalyst films in question. The approach suggested by the Bisquert group was employed in the characterization of the NiO-MB and the two NiO-NP films: transients were recorded in both non-aqueous and aqueous electrolyte solutions (0.10 M ferrocene in acetonitrile and a pH 9.20 borate buffer, respectively). Upon the application of a square wave potential signal (amplitude 0.50 V), current spikes are indicative of surface states. In the case of all three NiO films tested, no spikes were observed in the non-aqueous solution, while significant spikes were characteristic of the transient current response to potential disturbances in a pH 9.20 borate buffer solution (see Fig S9). This result indicated that a similar approach to that described by Bisquert and co-workers can be used in the EIS characterization of the NiO catalyst films.[44] The EC based on this model includes the following elements: space charge and Helmholtz double layer capacitances in series, referred to together as C_{bulk}; surface state (trap state) capacitance C_{tr}; series resistance, R_s; trap state resistance (R_{tr}, representing resistance caused by the recombination of charge carriers at the surface traps) and charge transfer resistance from the surface states to the electrolyte, $R_{ct,tr}$. This EC model was found to fit the impedance data well, when C_{bulk} was replaced by a constant phase element, CPE_{bulk} (see Figure 6). A CPE is commonly used to model the dielectric behaviour of electrical double layers and pseudocapacitors, acting as imperfect capacitors. Metal oxide electrodes generally have high pseudocapacitances, and nickel oxide porous films have also been used as supercapacitors.[45,46,47,48] Therefore, the CPE_{bulk} element considered more appropriate for modelling the dielectric capacitance of the NiO films than a pure capacitor.

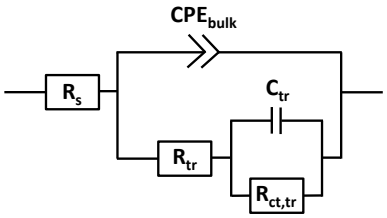

Figure 6: Equivalent circuit used for fitting EIS data

The chemical nature of the surface state capacitance (C_{tr}), has been discussed elsewhere,[49,50] and a peak in C_{tr} was shown to correspond to interfacial charge transfer, in this case, water oxidation.In the non-aqueous solution, C_{tr} for NiO is constant over a large potential window, as for other oxide films. As shown in Figure S10, C_{tr} was small and constant over a 1.00 V potential window when ferrocene was used as a hole collector in acetonitrile (measured versus an $Ag/AgNO_3$ pseudo-reference electrode). When measured in the pH 9.20 borate buffer, C_{tr} was found to have a Gaussian shape centred around 1.00 V *vs.* Ag/AgCl (Fig. S11). The Nyquist plots of fresh NiO-MB and NiO-NP films, measured at potentials from 0.40 V to 1.50 V at intervals of 0.10 V in 0.60 M borate buffer show two semicircles in the high frequency (first; at lower Re(*Z*)) and low frequency (second; at higher Re(*Z*)) region (Fig. 7). For all films, the second, lower frequency semicircle shows a significant reduction in radius with applied potential, especially at 1.00 V where the water oxidation reaction is apparent.

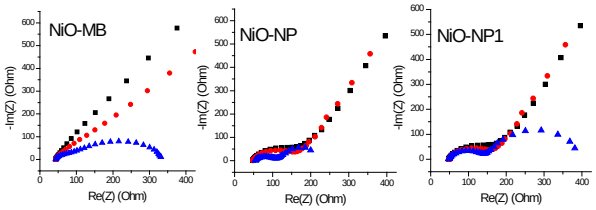

Figure 7: Electrochemical impedance spectroscopy (Nyquist plots) of fresh NiO-MB, NiO-NP and NiO-NP1 films in contact with 0.6 M NaB_i (pH = 9.2) at different potentials:0.50 V (black squares), 0.70 V (red dots) and 1.0 V vs Ag/AgCl (blue triangles).

EIS was also used to investigate the increase in activity of the films after anodization in the borate buffer solution. The impedance spectra of NiO-MB, NiO-NP and NiO-NP1 films in 0.60 M borate buffer are shown before and after anodization in Figures 8 A, B and C. After anodization, a distinctive reduction in the radius of the second semicircle can be observed, while little or no change was recorded in the radius of the first semicircle. This indicates that ageing mainly affected $R_{ct,tr}$, making the charge transfer from the catalyst to electrolyte more efficient. This correlates well with the higher current densities measured by CPE and LSV after anodization in borate buffer.

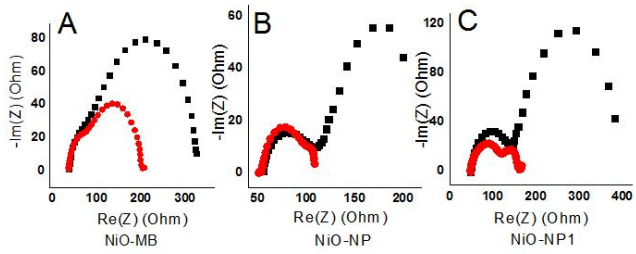

Figure 8: A, B and C: Nyquist plots of fresh (black squares) and anodized in 0.60 M NaB_i (pH = 9.2) (red dots) NiO MB, NP and NP1 films, respectively, recorded at 1 V *vs* Ag/AgCl in a 0.60 M NaBi buffer.

Two explanations have been provided to account for the increase in catalytic activity on ageing or anodization: (1) a change in the Ni oxidation state;[3,39,41] and (2) physical changes in the film (surface roughness).[31,6,41] The present results indicate that anodization causes a significant change in the R_{tr} for all films, and that there is a significant change in the nickel oxidation state on the catalyst surface (as analysed by XPS). The bulk remains mainly in the cubic NiO phase (as probed via *ex situ* XAS and XRD spectroscopy).

Conclusions

Films of cubic NiO nanoparticles and microballs, deposited by screen-printing, have been demonstrated to be very robust water oxidation catalysts when tested in borate buffer (pH 9.20) and alkaline solution (1.00 M NaOH). Notably, for the latter, current densities of 33 mA cm^{-2} were achieved at an overpotential of 0.60V. Impedance spectroscopy, and other analytical techniques, highlighted that parameters, such as the oxide film thickness, morphology and metal ion loading are important when optimizing catalytic performance in addition to the phase and metal oxidation state, and further confirmed the beneficial effect of anodization on the catalytic activity. EIS also emphasized the role of surface states in the catalytic process, in keeping with previous observations by the Bisquert group on photoactive hematite materials.[44,51] Resistance and capacitance data, extracted from the EIS analysis, were in good agreement with the catalytic activity observed for the three nickel oxide films.
Amorphous materials and layered structures are known to perform as efficient water oxidation catalysis but in the present study we demonstrate that highly crystalline, cubic NiO can also form the basis of a robust and efficient water oxidation electrocatalyst. The catalytic activity of the nickel oxide films was significantly improved by anodization, a process which was shown to generate a thin nanometer-sized layer of mixed nickel oxy-hydroxide on the film surface. This observation is consistent with other literature reports which have suggested that when electrochemical water oxidation catalysis is carried out in presence of applied bias then the activity of the bulk structure *vs* the outer surface exposed to the water should be considered carefully.[52-55] We believe that screen-printing offers the opportunity to use a wide array of materials to rapidly and controllably fabricate water oxidation catalysts on large areas for potential commercial use.

Experimental Section

Experimental

Materials and Methods:
Reagent or analytical grade chemicals were sourced from commercial suppliers and used as received unless stated otherwise. De-ionized water was used throughout. NiO microballs (NiO-MB) were synthesized by a thermolysis method as described before.[35] For comparison, water oxidation catalytic studies were also carried out on films prepared using commercially available NiO nanoparticles (NiO-NP, sourced from Inframat, 73.2 wt% Ni). The NiO-MB powder was ball-milled to enable preparation of a smooth screen-printing paste. The films were deposited using a screen-printing method following the similar procedure to that detailed in our previous publication.[35] In brief, 13.3 wt% of synthesized NiO-MBs and as received NiO-NPs were mixed with 40% ethyl cellulose solution (5 wt% in ethanol) and 46.7% terpineol. After preparing the mixture, the ethanol was evaporated by rotary evaporation and the pastes were subsequently printed on FTO glass using a semi-automatic screen printer. To prepare the NiO-MB film, a single layer of the paste was printed using a 90T mesh screen designed to print 25 4x4 mm^2 squares. The resulting films were sintered at 400 ˚C for 30 minutes and then 550 ˚C for 10 minutes. The NiO-NP paste was printed using the same method in a single layer (NiO-NP1) and in three layers (NiO-NP) to achieve similar thickness to the NiO-MB film. The thickness of the films was measured using a Veeco Dektak 6M stylus profilometer. The FTO sheet was then cut into rectangles of approx. 10x7 mm containing a NiO film each. Electrodes were made by soldering copper wire to the FTO glass.

Electrochemical techniques:
Measurements were performed in a three electrode cell using a BioLogic VSP potentiostat with Ag/AgCl as reference electrode, a Pt sheet as counter electrode and the NiO films as working electrode. The water oxidation activity testing was performed at room temperature. The potentials are referenced to the Ag|AgCl|KCl(3 M) (Ag/AgCl) reference electrode with no correction for Ohmic potential losses. Either a 0.60 M borate buffer solution, prepared by using appropriate quantities of H_3BO_3 and NaOH, or a 1.00 M NaOH solution was used as electrolyte.
Linear scan voltammograms were run in 0.60 M boratebuffer solutions at a scan rate of 20 mV/s to determine the current *vs* potential profiles of the films. Long term testing was performed at 1.10 V *vs* Ag/AgCl for 12 hours of continuous operation. The films were tested in H-shaped cell with continuous stirring. The NiO-films, together with reference electrode were placed in one arm of the cell, while the counter electrode was located in the other arm of the cell. A Tafel plot was constructed from stepwise chronoamperometry data, which was measured after holding the potential constant at each potential step for two minutes to ensure a stable current was obtained. The chronoamperogram was recorded in the anodic as well as the cathodic direction. The average of the cathodic and anodic peaks was used to construct Tafel plots. Oxygen detection was performed in a custom built three-electrode electrochemical cell with the NiO-MB as working electrode, Ag/AgCl as reference electrode and Pt mesh as counter electrode. The experiment was performed at an applied potential of 1.10 V *vs* Ag/AgCl in a low-oxygen glove box at atmospheric pressure. Oxygen was detected in the headspace of the electrochemical cell using a NeoFox fluorescence-quenching oxygen sensor. The values obtained were corrected by accounting for the dissolved oxygen determined by Henry's law.[34]
Electrochemical impedance spectroscopy measurements were carried out in a Zahner PECC-I cell where the distance

between the working electrode and reference electrode was constant for all the films to improve accuracy of the measurements. Impedance spectra were recorded between 0.40 V and 1.50 V (with 0.10 V increments) in a 0.60 M borate buffer *vs* Ag/AgCl reference electrode between frequencies of 1 MHz to 100 mHz using an amplitude of 10 mV. EIS measurements were also carried out in acetonitrile with 0.10 M ferrocene using a $Ag/AgNO_3$ (CH_3CN) system as a pseudo-reference electrode. The working electrode area was 0.16 cm^2.

Characterization Methods: The structure and morphology of the films were studied by SEM, TEM, XPS, XAS and XRD techniques. SEM images of the films before and after water oxidation studies were recorded on a FEI Nova FEG-SEM at a working distance of 5 mm at 5 keV beam landing energy. The films were previously sputter-coated with a 1 nm thick layer of iridium. To compare the surface morphology of films before and after anodization, the films were electrolyzed in 0.60 M borate buffer at 1.10 V continuously for twelve hours and then used to record SEM images. TEM images and diffraction patterns were recorded on a Tecnai T20 instrument operated at 200 keV. Powder XRD patterns were recorded on a Philips instrument (2θ = 10°-90°). XPS analysis was performed on an AXIS Ultra DLD X-ray photoelectron spectrometer (Kratos Analytical, Manchester, U.K.) using a monochromatic Al Ka source and the standard aperture (analysis area: 0.70 mm × 0.30 mm). Survey spectra were acquired at a pass energy of 160 eV. To obtain more detailed information about chemical structure, oxidation states etc., high resolution spectra were recorded from individual peaks at 20 eV pass energy. Each specimen was analyzed at an emission angle of 0° as measured from the surface normal. Assuming typical values for the electron attenuation length of relevant photoelectrons, the XPS analysis depth ranges between 5 and 10 nm for a flat surface. XPS survey spectra were quantified by integrating relevant peaks (e.g. Ni 2p, O 1s) after subtraction of a Shirley background, then applying appropriate relative sensitivity factors (provided by the manufacturer) to the peak areas (e.g. 4.044 for Ni 2p, 0.78 for O 1s, all relative to 1.0 for F 1s).To determine their Ni-content, each film was dissolved in aqua regia, and then analyzed by inductively coupled plasma–time of flight-mass spectrometry (ICP-TOF-MS) using a GBC Optimass 9500 instrument, following a similar procedure to that used in our previous work.[34] Brunauer-Emmett-Teller (BET) surface area measurements (N_2 absorption-desorption analysis) were conducted on a Micrometrics Tristar 3000 equipment. The relative electrochemical surface area (given as cm_e^2) over the geometric surface area (cm_g^2) of the three films was calculated from the BET and ICP-MS data: A_{echem} [$cm_e^2 cm_g^{-2}$] = Ni content [mg/cm_g^2] x BET surface area [cm_e^2/mg].
Ni K-edge XAS spectra were recorded on the multipole wiggler XAS beam-line 12 ID at the Australian Synchrotron, in operational mode 1.[36] The beam energy was 3.00 GeV and the maximum beam current was 200 mA. The energy scale was calibrated using a Ni foil as an internal standard where the calibration energy of 8333.0 eV corresponds to the first inflection point of the foil. The Average program,[37]was used to average raw data files, and exclude channels. Fluorescent mode XAS data were taken directly on the electrodes at room temperature. The program PySpline[38]was used to subtract background data, spline the data and calculate the Fourier transform of the EXAFS. An E_0 value of 8340 eV was used when defining the k-range of the EXAFS. A four-segment spline of order 2 was fit to the EXAFS region, and all data normalized to the edge jump at 8370 eV.

Acknowledgements: Financial support by the Australian Research Council (ARC), through the ARC Centre for Excellence for Electromaterials Science, is gratefully acknowledged. AS is grateful to Monash University for a Monash Graduate Research Scholarship and an International Postgraduate Research Scholarship. AS is also grateful for financial assistance provided through an INSPIRE Faculty award, DST, India. The authors acknowledge the use of facilities in the Monash Centre for Electron Microscopy. Access to equipment and assistance from Dr M. Raveggi (School of Geosciences, Monash University) is greatly appreciated. Part of this research was undertaken on the X-ray absorption spectroscopy beamline at the Australian Synchrotron, Australia.

Keywords: Nickel oxide •screen printing • nanostructure • thin films •water oxidation catalysis.

References

[1] D. G. Nocera, *Daedalus-Us,***2006**, *135*, 112-115.
[2] N. S. Lewis, D. G. Nocera, *P. Natl. Acad. Sci. USA***2006**, *103*, 15729-15735.
[3] D. K. Bediako, B. L. Kaiser., Y. Surendranath, J. Yano, V. K. Yachandra, D. G. Nocera, *J. Am. Chem. Soc.***2012**, *134*, 6801-6809.
[4]a) J. G. McAlpin, T. A. Stich., C. A. Ohlin, Y. Surendranath, D. G. Nocera, W. H. Casey, R. D. Britt, *J. Am. Chem. Soc.***2011**, *133*, 15444-15452. b) D. Wang, G. Ghirlanda, J.P. Allen, *J. Am. Chem. Soc.***2014**, *136*, 10198-10201. c) K. Sun, X. Pang, S. Shen, X. Qian, J. S. Chang, D. Wang, *Nano Lett.***2013**, *13*, 2064-2072. d) D. Hong, Y. Yamada, T. Nagatomi, Y. Takai, S. Fukuzumi, J. *Am. Chem. Soc.***2012**, *134*, 19572-19575. e) M. Gao, . Sheng, Z. Zhuang, Q. Fang, S. Gu, J. Jiang, Y. Yan, *J. Am. Chem. Soc.*, **2014**, *136*, 7077-7084.
[5] M. D. Symes, Y. Surendranath, D. A. Lutterman, D. G. Nocera, *J. Am. Chem. Soc.***2011**, *133*, 5174-5177.
[6] M. Dinca, Y. Surendranath, D. G. Nocera, *Proc. Natl. Acad. Sci. U.S.A.***2010**, 10337-10341.
[7] M. W. Kanan, D. G. Nocera, *Science***2008**, *321*, 1072-1075.
[8] S. Y. Reece, J. A. Hamel, K. Sung, T. D. Jarvi, A. J. Esswein, J. J. H. Pijpers, D. G. Nocera, *Science***2011**, *334*, 645-648.
[9] Y. Surendranath, M. W. Kanan, D. G. Nocera, *J. Am. Chem. Soc.***2010**, *132*, 16501-16509.
[10] Y. Surendranath, D. A. Lutterman, Y. Liu, D. G. Nocera, *J. Am. Chem. Soc.***2012**, *134*, 6326-6336.
[11] G. C. Dismukes, R. Brimblecombe, G. A. N. Felton, R. S. Pryadun, J. E. Sheats, L. Spiccia, G. F. Swiegers, *Accts. Chem. Res.***2009**, *42*, 1935-1943.
[12] R. Brimblecombe, A. Koo, G. C. Dismukes, G. F. Swiegers, L. Spiccia, *ChemSusChem***2010**, *3*, 1146-1150.
[13] R. Brimblecombe, A. Koo, G. C. Dismukes, G. F. Swiegers, L. Spiccia, *J. Am. Chem. Soc.***2010**, *132*, 2892-2894.

[14] R. Brimblecombe, A. M. Bond, G. C. Dismukes, G. F. Swiegers, L. Spiccia, *PhysChemChemPhys***2009**, *11*, 6441-6449.
[15] R. Brimblecombe, G. F. Swiegers, G. C. Dismukes, L. Spiccia, *Angew. Chem. Int. Ed.,***2008**, *47*, 7335-7338.
[16] R. K. Hocking, R. Brimblecombe, L. Y. Chang, A. Singh, M. H. Cheah, C. Glover, W. H. Casey, L. Spiccia, *Nat. Chem.***2011**, *3*, 461-467.
[17] M. Risch, K. Klingan, J. Heidkamp, D. Ehrenberg, P. Chernev, I. Zaharieva, H. Dau, *Chem. Commun.* **2011**, *47*, 11912-11914.
[18] M. Gratzel, *Nature***2001**, *414*, 338-344.
[19] K. Sivula, F. Formal, M. Gratzel, *ChemSusChem***2011**, *4*, 432-449.
[20] M. Risch, K. Klingan, J. Heidkamp, D. Ehrenberg, P. Chernev, I. Zaharieva, H. Dau, *Chem. Commun.***2011**, *47*, 11912-11914.
[21] M. Risch, I. Zaharieva, L. Gerencser, P. Chernev, H. Dau, *J. Am. Chem. Soc.***2009**, *131*, 6936-6937.
[22] M. M. Najafpour, V. McKee, *Catal. Commun.***2010**, *11*, 1032-1035.
[23] M. M. Najafpour, W. Hillier, A. N. Shamkhali, M. Amini, K. Beckman, Z. Jaglicic, M. Jagodic, P. Strauch, A. N. Moghaddam, G. Beretta, M. Bagherzadeh, *Dalton Trans.***2012**, *41*, 12282-12288.
[24] M. Najafpour, S. Nayeri, B. Pashaei, *Dalton Trans.* **2011**, *40*, 9374-9378.
[25] M. Najafpour, *Dalton Trans.* **2011**, *40*, 3805-3807.
[26] P. Kurz, G. Berggren, M. F. Anderlund, S. Styring, *Dalton Trans.***2007**, *38*, 4258-4261.
[27] K. Beckmann, H. Uchtenhagen, G. Berggren, M. F. Anderlund, A. Thapper, J. Messinger, S. Styring, P. Kurz, *Energy Environ. Sci.* **2008**, *1*, 668-676.
[28] B. E. Conway, L. Bai, *Int .J. Hydrogen Energy***1986**, *11*, 533-538.
[29] J. Y. Huor, M. Trudeau, L. Brossard, R. Schulz, *Int. J. Hydrogen Energy***1989**, *14*, 319-323.
[30] P. Oliva, J. F. Laurent, *J. Power Sources***1982**, *8*, 229-255.
[31] M. R. Chialvo, A. C. Chialvo, *Electrochim. Acta***1988**, *33*, 825-830.
[32] K. Sun, N. Park, Z. Sun, J. Zhou, J. Wang, X. Pang, S. Shen, S. Y. Noh, Y. Jing, S. Jin, P. K. L. Yua, D. Wang, *Energy Environ. Sci***2012**, *5*, 7872-7877.
[33] X. Wanga, H. Yang, P. J. Sebastian, S. A. Gamboa, *Int. J. Hydrogen Energy***2004**, *29*, 967-972.
[34] A. Singh, S. Chang, R. K. Hocking, U. Bach, L. Spiccia, *Energy Environ. Sci***2013**,6, 579-586.
[35] S. Powar, Q. Wu, M. Weidelener, A. Nattestad, Z. Hu, A. Mishra, P. Bauerle, L. Spiccia, Y. Cheng, U. Bach, *Energy Environ. Sci***2012**, 5, 3280-3283.
[36] A. Zouni, W. Horst-Tobias, J. Kern, P. Fromme, N. Krauss, W. Saunger, P. Orth, *Nature***2000**, 409, *739-743*.
[37] W. L. Butler, M. Kitajima, *Biochim. Biophys. Acta***1975**, *396*, 72-85.
[38] A. Tenderholt, B. Hedman, K. O. Hodgson, In *XAFS13*; AIP: Stanford California, 2007; Vol. 882, p 105.
[39] B. S. Yao, A. T. Bell, *J. Phys. Chem. C***2012**, *116*, 8394-8400.
[40] C. K. Dyer, *J. Electrochem. Soc.***1985**, *132*, 64-67.
[41] M. E. G. Lyons, M. P. Brandon, *Int. J. Electrochem. Sci.***2008**, *3*, 1386-1424.
[42] N. Srivastava, P. C. Srivastava, *Bull. Mater. Sci.***2010**, *33*, 653-656.
[43] M. C. Biesinger, B. P. Payne, L. W. M. Lau, A. Gerson, R. St. C. Smart, *Surf. Interface Anal.***2009**, *41*, 324-342.
[44] B. Klahr, S. Gimenez, F. Fabregat-Santiago, T. Hamann, J. Bisquert, *J. Am. Chem. Soc,***2012**, *134*, 4294-4302.
[45] X. Xia, J. Tu, Y. Zhang, X. Wang, C. Gu, X. Zhao, H. J. Fan, *ACS Nano,***2012**, *6*, 5531-5538.
[46] C. Yuan, X. Zhang, L. Su, B. Gao, L. Shen, *J. Mater. Chem.***2009**, *19*, 5772-5777.
[47] X. Zhang, W. Shi, J. Zhu, W. Zhao, J. Ma, S. Mhaisalkar, T. L. Maria, Y. Yang, H. Zhang, H. H. Hng, Q. Yan, *Nano Res.* **2010**, *3*, 643-652.
[48] http://www.easyspin.org/.
[49] J. Bisquert, *PhysChemChemPhys***2003**, *5*, 5360-5364.
[50] J. Bisquert, *PhysChemChemPhys.***2008**, *10*, 49-72.
[51] B. Klahr, S. Gimenez, F. Fabregat-Santiago, T. Hamann, J. Bisquert, T. W. Hamann, *J. Am. Chem. Soc.***2012**, *134*, 16693-16700.
[52] P. W. Menzes, A. Indra, P. Littlewood, M. Schwarze, C. Gobel, R. Schomacker, M. Driess, *ChemSusChem*, **2014**, *7*, 2202-2211.
[53] A. Indra, P. W. Menzes, M. Driess, *ChemSusChem*, **2015**, *8*, 776-785.
[54] D. Gonzalez-Flores, I. Sanchez, I. Zaharieva, K. Klingan, J. Heidkamp, P. Chernev, P. W. Menzes, M. Driess, H. Dau, M. L. Montero, *Angew. Chem. Int. Ed.*, **2015**, *54*, 2472-2476.
[55] P. W. Menzes, A. Indra, D. Gonzalez-Flores, N. R. Schraie, I. Zaharieva, M. Schwarze, P. Strasser, H. Dau, M. Driess, *Acs Catal*., **2015**, *51*, 2017-2027.

Entry for the Table of Contents

Thin films of NiO nanoparticles and microballs are demonstrated to be efficient and highly robust water oxidation catalysts, and their performance shown to improve with anodization.

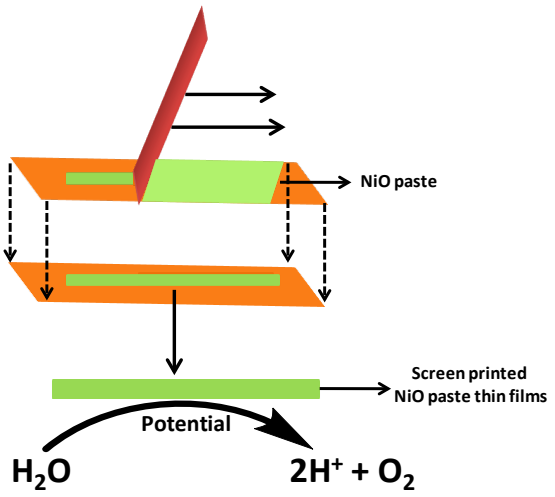

Archana Singh, Monika Fekete, Thomas Gengenbach, Alexandr N Simonov, Rosalie K. Hocking, Shery L. Y. Chang, Mathias Rothmann, Satvasheel Powar, Dongchuan Fu, Zheng Hu, Qiang Wu, Yi-Bing Cheng, Udo Bach and Leone Spiccia**